CMOS photonic integrated circuit for flex-grid polarization entanglement

Alexander Miloshevsky,[1,†] Hsuan-Hao Lu,[1] Lucas M. Cohen,[2]
Karthik V. Myilswamy,[2] Saleha Fatema,[2] Muneer Alshowkan,[1]
Andrew M. Weiner,[2] and Joseph M. Lukens[1,3]

[1]*Quantum Information Science Section, Computational Sciences and Engineering Division, Oak Ridge National Laboratory, Oak Ridge, Tennessee 37831, USA*
[2]*School of Electrical and Computer Engineering and Purdue Quantum Science and Engineering Institute, Purdue University, West Lafayette, Indiana 47907, USA*
[3]*Research Technology Office and Quantum Collaborative, Arizona State University, Tempe, Arizona 85287, USA*
[†]*miloshevskya@ornl.gov*

Abstract: We showcase a CMOS-fabricated silicon photonic integrated circuit employing a bidirectionally pumped microring and polarization splitter-rotators for high-fidelity polarization entanglement. Spanning the optical C+L-band, this sources is ideal for wavelength-multiplexed entanglement distribution in multi-user networks.

Quantum networks of the future [1] will need to be flexible to provide on-demand entanglement distribution for multiple end-users, adapt to user data requirements, and maneuver unexpected disruptions to communication channels. To this end, recent experiments combining broadband polarization entanglement with wavelength-selective switches (WSSs) chart a promising path forward [2–4]. Leveraging concepts proven in classical "flex-grid" or "elastic" optical networking [5], the center wavelength, bandwidth, and lightpath of any quantum demand can be reconfigured adaptively and by request. In this paradigm, broadband and compact polarization-entangled sources are of critical importance, yet fully on-chip devices that are CMOS-compatible and support ultradense channel spacings are currently lacking. In this work, we present a novel on-chip source for flex-grid quantum networking that features an on-chip bidirectionally pumped microring resonator (MRR) with integrated polarization splitter-rotators for wavelength-multiplexed entanglement distribution. We verify high-fidelity operation through quantum state tomography (QST) of 116 individual channel pairs and various channel groupings, confirming the viability of flexible bandwidth allocations. Our broadband, compact, and mass-producible source has the potential to tolerate increased link losses or adapt to evolving bandwidth requirements of individual end-users.

Figure 1(a) illustrates the on-chip polarization-entanglement source design. The die, designed for and manufactured by the AIM Photonics multi-project wafer service [6], features a central MRR sandwiched by a pair of on-chip polarization splitter-rotators (PSRs). The first PSR spatially separates the input light according to polarization—transverse electric (TE) or transverse magnetic (TM)—and rotates the TM portion to a TE output. These pump photons are bidirectionally coupled into the MRR, enabling the generation of entangled photon pairs through spontaneous four-wave mixing (SFWM) in both directions. The photon pairs, along with the pump photons, are TE-polarized. In addition, signal and idler photons exhibit energy-time entanglement across multiple pairs of resonances defined by the MRR, which is designed with a free spectral range of 38.4 GHz and intrinsic (loaded) Q factors of 3.7×10^5 (3.7×10^4). Once the photons are extracted from the MRR, a second PSR converts one pathway back to TM polarization before recombining with the unrotated TE pathway. In the ideal scenario, the output is an equal coherent superposition of two counterpropagating SFWM processes, as depicted in Fig. 1(b), where each pair of energy-matched resonances manifests a polarization Bell state $|\Phi^+\rangle = \frac{1}{\sqrt{2}}(|H_{\omega_k}H_{\omega_{-k}}\rangle + |V_{\omega_k}V_{\omega_{-k}}\rangle)$. Here, TE (TM) is analogous to horizontal H (vertical V) polarization, and the integer $k \geq 1$ denotes the frequency bin (number of resonances away from the pump).

Figure 1(c) illustrates our experimental setup for generating and characterizing the wavelength-multiplexed polarization entangled state. We operate a tunable continuous-wave laser (Santec TSL-570) to pump the chip, aligning the pump wavelength with one of the ring resonances at ∼1559.85 nm. To attenuate the background noise in the pump laser, we incorporate three dense wavelength division multiplexers (DWDMs): two with a 100 GHz

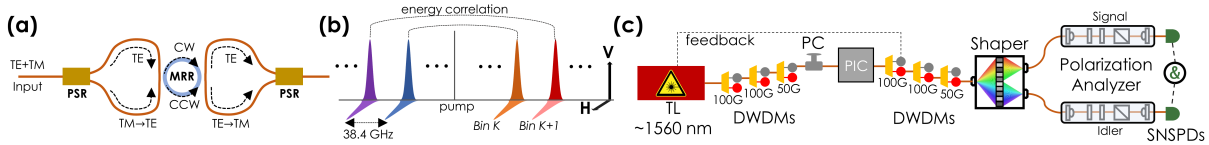

Fig. 1. (a) Schematic of the quantum PIC design. (b) Conceptual diagram of the wavelength-multiplexed polarization-entangled source. (c) Experimental setup. [TE: transverse electric; TM: transverse magnetic; MRR: microring resonator; TL: continuous-wave tunable laser; DWDMs: dense wavelength-division multiplexers; PC: polarization controller; PIC: photonic integrated circuit; PSR: polarization splitter-rotator; SNSPD: superconducting nanowire single photon detector.

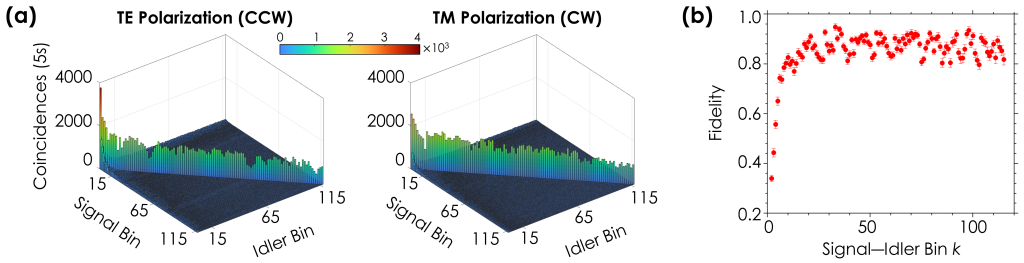

Fig. 2. (a) The unidirectionally pumped JSI (1 ns coincidence window), measured for bins $k \in \{2,...,117\}$ for each photon. (b) Bayesian state fidelities for the 116 energy-matched pairs in (a).

passband and one with a 50 GHz passband, all centered around 1559.81 nm. Following the DWDMs, a polarization controller (PC) manages the ratio of TE and TM polarization before coupling the pump light (∼10 dBm) into the chip. Upon exiting the chip, another set of three DWDMs, replicating the prior configuration, isolates the newly generated broadband entangled photons from the residual pump light, with an estimated pump suppression of ∼68 dB. Additionally, we implement a feedback loop that monitors the optical power in the pass channel of the first output DWDM, ensuring the pump aligns with the intended cavity resonance in the presence of any real-time thermal drift. Finally, we employ a Fourier-transform pulse shaper (Finisar Waveshaper 4000B) as a WSS to route two frequency bins, one from the signal side of the spectrum and one from the idler, to two separate optical fibers for subsequent state characterization. Two-qubit polarization QST is carried out using a pair of motorized polarization analyzers (consisting of a quarter-wave plate, a half-wave plate, and a polarizing beamsplitter cube) followed by photon detection with superconducting nanowire single-photon detectors (Quantum Opus) connected to a photon-counting module (PicoQuant TimeHarp).

We first characterize our MRR source by measuring the joint-spectral intensity (JSI) under unidirectional pumping. We tune the PC to excite only the TE or TM polarization into the chip, bypass both polarization analyzers, and program the pulse shaper to scan through a total of 116×116 frequency-bin combinations for coincidence measurements ($k \in \{2,...,117\}$; the first bin pairs are clipped by the DWDMs), as shown in Fig. 1(a). The ∼10 closest pairs experience noticeably higher accidental coincidences from residual pump light, which would necessitate additional DWDMs after the chip for further noise reduction. Measured coincidences for matched pairs remain steady across the >100 channels analyzed (averaging 1100 ± 200 coincidences for TE and 1300 ± 300 for TM, per 5 s), periodically dipping due to coupling misalignment. We compute the average coincidence-to-accidental ratio (CAR) to be 230 ± 90 (300 ± 100) for TE (TM). No significant decrease in coincidence counts was observed within the C+L-band pulse shaper's acceptance bandwidth (1530–1625nm), indicating low dispersion enabling ultrabroad biphoton bandwidth. However, to comprehensively analyze our design, it would be necessary to incorporate additional components tailored for the S-band (1460–1530nm) and longer wavelengths (>1625 nm).

We conduct polarization QST on these 116 energy-matched bin pairs by adjusting the pump polarization such that the pair generation probabilities are balanced between the two counterpropagating processes. We scan through a total of 36 polarization projections, collecting coincidence counts (30 s per projection) for subsequent Bayesian state analysis [7,8]. For each bin pair, we infer a total of 1024 density matrix samples from the gathered dataset, enabling the calculation of quantum state fidelity and other entanglement metrics. The fidelities with respect to $|\Phi^+\rangle$ are depicted in Fig. 2(c). As expected, fidelities are lower for channels closer to the pump frequency but steadily improve as the channel separation increases, reaching a plateau that remains in the range of approximately 0.80 to 0.95 across the rest of the spectrum. The cause of the fluctuations in this region is currently under investigation, but could be due to polarization or coupling drifts during the full measurement procedure. The average fidelity for all bins is $(85 \pm 9)\%$, increasing to $(87 \pm 4)\%$ when excluding the first 10.

Finally, we delve into the possibilities of utilizing this source for adaptive wavelength-multiplexed entanglement distribution. As an example, we consider a simplified one-link model [9] within a flex-grid network [2–4] where a central source node connects to multiple destination nodes (users), each featuring distinct link characteristics, such as channel losses and detector efficiencies. Leveraging flex-grid technologies like pulse shapers or WSSs, the broadband biphoton spectrum can be dynamically partitioned into numerous pairs of energy-correlated bands. These pairs are then routed to network users, guaranteeing that each user establishes an entangled connection with a desired counterpart, thus enabling the central node to deliver quantum services. In the simplest scenario, one frequency bin pair could be assigned to each pair of users, which for our source would mean the support of high-fidelity entanglement for more than 100 pairs of nodes [cf. Fig. 2(c)], constrained only by the WSS passband and number of output fibers.

When certain users contend with increased link losses or seek additional services, we also have the flexibility to group adjacent bins together for reallocation, effectively enhancing the coincidence rate. However, expanding the bandwidth of each entangled pair may compromise polarization entanglement due to increased sensitivity to

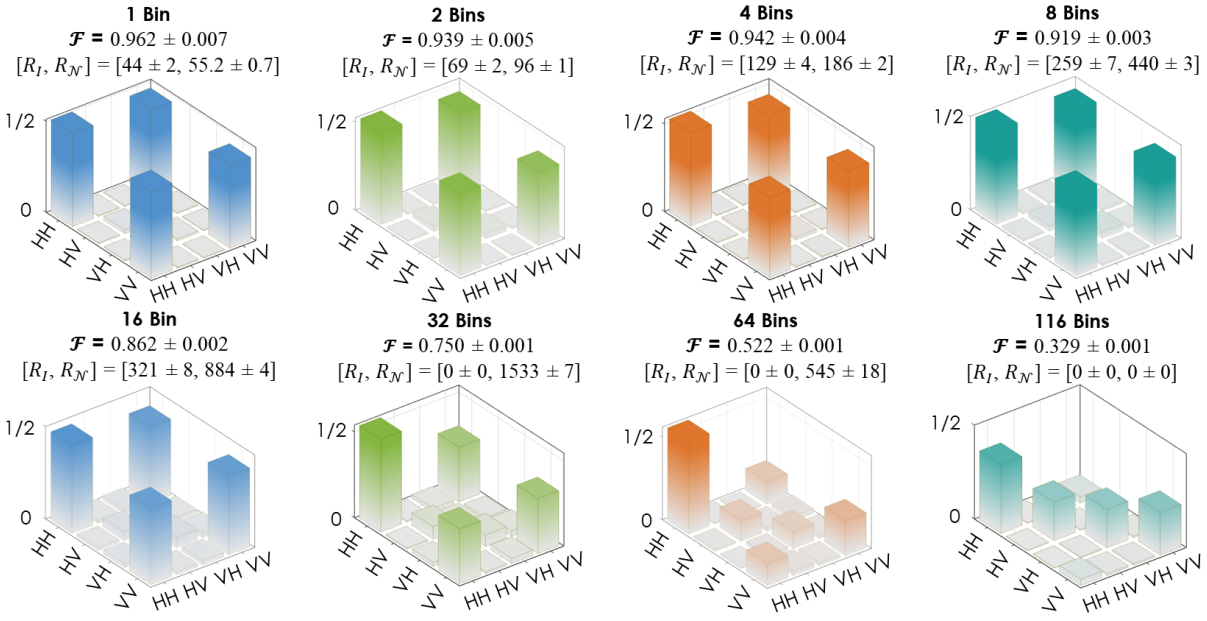

Fig. 3. The polarization density matrix, fidelity, and lower and upper bound of the entangled bit rate (EBR) for various number of bin groupings obtained from Bayesian tomography.

polarization-mode dispersion, and the CAR will reduce as well, simply from the increased flux and hence higher multipair-induced accidentals [9] Consequently, striking a balance between these competing factors—optimizing throughput while upholding entanglement quality above a predefined, application-specific threshold—emerges as a matter well worth investigating. Figure 3 provides an initial glimpse into this investigation, illustrating how bin grouping impacts state quality as evaluated through polarization QST. Our approach involves initially passing one bin on each side of the spectrum ($k = 58$) and symmetrically widening the filter passband, resulting in output states comprised of 2, 4, 8, 16, etc. consecutive frequency bins. As anticipated, state fidelity decreases with larger bin groupings, while the coincidence rate rises, a tradeoff which we can quantify through the entangled bit rate (EBR) defined as the distillable entanglement times the coincidence rate [10]. Lower and upper bounds on EBR, $[R_I, R_{\mathcal{N}}]$, can be obtained from the coherent information and log-negativity, respectively, which we include in Fig. 3. In general, EBR increases as bins are grouped together due to the rising flux but eventually decreases as the polarization state becomes increasingly mixed. These findings show the flexibility of our compact design to adapt to end-user demands and varying channel conditions.

This work was performed in part at Oak Ridge National Laboratory, operated by UT-Battelle for the U.S. Department of Energy under contract no. DE-AC05-00OR22725. The Quantum Collaborative, led by Arizona State University, provided valuable expertise and resources for this work. Funding was provided by the U.S. Department of Energy, Office of Science, Advanced Scientific Computing Research (ERKJ353, ERKJ378) and the National Science Foundation (ECCS-2034019).

References

1. S. Wehner, D. Elkouss, and R. Hanson, *Science* **362**, eaam9288 (2018).
2. N. B. Lingaraju, H.-H. Lu, S.Seshadri, D. E. Leaird, A. M. Weiner, and J. M. Lukens, *Optica* **8**, 329 (2021).
3. F. Appas, F. Baboux, M. I. Amanti, A. Lemaítre, F. Boitier, E. Diamanti, and S. Ducci, *npj Quantum Inf.* **7**, 118 (2021).
4. M. Alshowkan, B. P. Williams, P. G. Evans, N. S. Rao, E M. Simmerman, H.-H. Lu, N. B. Lingaraju, A. M. Weiner, C. E. Marvinney, Y.-Y. Pai, B. J. Lawrie, N. A. Peters, and J. M. Lukens, *PRX Quantum* **2**, 040304 (2021).
5. O. Gerstel, M. Jinno, A. Lord, and S. J. Ben Yoo, *IEEE Commun. Mag.* **50**, S12–S20 (2012).
6. N. M. Fahrenkopf, C. McDonough, G. L. Leake, Z. Su, E. Timurdogan, and D. D. Coolbaugh, *IEEE J. Sel. Top. Quantum Electron.* **25**, 8201406 (2019).
7. R. Blume-Kohout, *New J. Phys.* **12**, 043034 (2010).
8. J. M. Lukens, K. J. H. Law, A. Jasra, and P. Lougovski, *New J. Phys.* **22**, 063038 (2020).
9. J. Alnas, M. Alshowkan, N. S. V. Rao, N. A. Peters, and J. M. Lukens, *Opt. Express* **30**, 24375 (2022).
10. M. Alshowkan, J. M. Lukens, H.-H. Lu, B T. Kirby, B P. Williams, W P. Grice, and N. A. Peters, *Opt. Lett.* **47**, 6480 (2022).